



A Unified Computational Formulation for Multi-Component and Multi-Phase Flows

Ding Li * and Venkateswaran Sankaran †

Purdue University, West Lafayette, IN 47906

Jules W. Lindau ‡

Applied Research Lab/Penn State, State College, PA 16804

Charles L. Merkle §

Purdue University, West Lafayette, IN 47906

A unified computational formulation for homogeneous mixture flows involving multiple phases and multiple species is presented. The formulation is based upon using a generalized equation of state that is valid for arbitrary fluids, including liquids, gases and supercritical fluids. Thermodynamic properties of the mixture are uniformly determined by using Amagat's law rather than Dalton's law for liquid-gas, liquid-liquid or gas-gas mixtures. Proper system conditioning for implementation of standard numerical procedures is obtained using appropriate scaling of the pseudo-time-stepping scheme. The capabilities of the approach are demonstrated using several applications involving multi-phase and multi-component mixture flows such as hydrodynamic cavitation, real gas nozzle flows, reacting flows and underwater propulsion.

I. Introduction

An emerging area of importance in computational modeling involves the simulation of multiple-component gas, liquid and solid mixtures. Such multi-component and multi-phase flows are encountered in a wide variety of applications involving cavitation, liquid sprays, combustion and real-gas flows. Numerous levels of physical modeling have been proposed to tackle such flowfields, ranging from the continuum-based Eulerian techniques, Lagrangian methods and various surface-tracking approaches¹ to microscopic and mesoscopic approaches such as particle dynamics and Lattice-Boltzmann techniques.² In this paper, we are concerned with a class of continuum-Eulerian methods, which are normally referred to as homogeneous-mixture models.

For a liquid-gas mixture in an Eulerian-Eulerian framework, the homogeneous-mixture model assumes that the gas-liquid interface is in dynamic and thermal equilibrium and, consequently, mixture momentum and energy equations can be used to describe the flowfield. To represent the phase-change phenomena as well as gas-phase chemical reactions, separate continuity equations are employed for the liquid and gaseous components. Such a model is appropriate for flows involving large discrete liquid and gas-phase regions with negligible surface tension effects. Typical applications of interest to the present authors, which permit such a level of approximation, include attached sheet cavitation, wind tunnel and nozzle condensation, combustion, liquid film cooling in rocket combustors and underwater propulsion systems. Some of these problems involve multiple phases, others involve gaseous mixtures and still others require the simultaneous consideration of multiple phases and multiple gaseous species. The focus of the present paper is the development of a unified computational framework for arbitrary liquid and gas mixtures so that same formulation may be applied for such diverse classes of problems.

*Senior Researcher, Member AIAA

†Senior Researcher, Member AIAA

‡Research Associate, Member AIAA

§Vincent P. Riley Professor of Engineering, Member AIAA

Several researchers have formulated methods for solving arbitrary fluids, multi-component gaseous mixtures and multiple phases. Merkle et al.³ and Weiss et al.⁴ have developed a pseudo-time-iterative method using preconditioning for arbitrary fluids or general equations of state. The preconditioning formulation adapts the eigenvalues of the time-marching system to be well-conditioned for all speeds, which is important for purposes of the numerical discretization and solution procedure.⁵ Several researchers have also developed methods for multi-component gaseous mixtures⁶ as well as for multi-phase mixtures.⁷⁻¹³ Recently, Lindau et al.¹⁴ have extended their method to simultaneously handle both multi-component gaseous and liquid mixtures. These publications demonstrate the rapid maturation of computational capabilities, but the underlying methods typically use different approaches for gaseous species and liquid phases, which complicates code development and implementation for general problems.

Mixtures of perfect gases are usually represented by Dalton's Law,¹⁵ which envisions that the different species components occupy the same volume and are at the same temperature, but exert different partial pressures. Liquid-gas mixtures, on the other hand, are traditionally described by Amagat's mixture model,¹⁵ which postulates that the liquid and gas components occupy separate and distinct partial volumes, but exist at the same pressure and temperature. The two different approaches naturally give rise to distinct formulations, which complicates their implementation and application. Moreover, Dalton's law is limited to perfect gas mixtures and it is not straightforward to extend it to real gases and arbitrary mixtures. In this paper, we show that Amagat's law provides a framework for unifying multiple gaseous species and phases. It is identical to Dalton's law for perfect gas mixtures, while it is also capable of handling mixtures of fluids, both liquids and gases, each governed by arbitrary equations of state. The resulting formulation is more compact, easy to implement into existing CFD codes and applicable to a wide range of practical flowfields.

The present paper is organized as follows. We first present the equations of motion for multiple species or phases using a common notation. We then describe various approaches for determining the thermodynamic mixture property definitions: first, the standard Dalton's law for perfect gas mixtures and the standard Amagat's law for pure liquid mixtures. In particular, we show that Amagat's law may be readily extended to perfect and real gas mixtures, making it the ideal basis for a unified formulation for both liquids and gases. We then present representative flowfield solutions related to several applications of current interest to us. These include hydrodynamic cavitation, real-gas nozzle flows, reacting combustor flows and underwater propulsive flows. The wide range of results demonstrate the general applicability of the formulation to the problems of interest.

II. Theoretical Formulation

A. Equations of Motion

The 3D Navier-Stokes equations for N species or phasic components may be written as:

$$\frac{\partial Q}{\partial t} + \frac{\partial E_i}{\partial x_i} = H + \frac{\partial V_i}{\partial x_i} \quad (1)$$

where the flux vectors Q , E_i and V_i have their usual definitions and H is the source term vector. For definiteness, the inviscid flux vectors are defined below:

$$Q = \begin{pmatrix} \rho \\ \rho u_j \\ e \\ \rho Y_m \end{pmatrix} \quad E_i = \begin{pmatrix} \rho u_i \\ \rho u_i u_j + p\delta_{ij} \\ (e + p)u_i \\ \rho u_i Y_m \end{pmatrix}$$

where m stands for the liquid and/or gaseous species components. Note that the first equation represents the global continuity equation in the standard form. Therefore, we require $(N - 1)$ individual component transport equations, where N is the number of gaseous/liquid species components in the system. The N th species component is obtained by the definition that the sum of the mass fractions must equal unity. Thus, we have:

$$Y_N = 1 - \sum_{N-1} Y_m \quad (2)$$

Alternately, the global continuity equation in the first row may be replaced by one of the species components, say the liquid species. Also, the phasic equations are often written in terms of the individual volume

fractions. While these are common choices in most multi-phase codes, we note that there are no fundamental numerical reasons for favoring these choices. In our development, we retain the use of the overall continuity equation and the mass fraction variables. We note however that the numerical formulation developed here may be adapted to these alternate systems as well, although as discussed in our earlier work,⁹ some of these choices can lead to considerable algebraic complexity.

The above system of equations is closed by the equations of state, that describe the thermodynamics properties of the constituent species or phases, and appropriate mixture rules for determining the properties of the mixture. For each component two thermodynamic properties are required to fix the state of that species or phasic component. In addition, the mass or volume fraction of each component is required to specify the mixture properties. In general, there are two possible mixture laws: Gibbs-Dalton law and Amagat's law. The former is commonly used in the case of gaseous mixtures and the latter is used for liquid-vapor systems. We start by describing each of these laws in turn and then argue that Amagat's law provides the basis for a unified formulation for both multi-species and multi-phase mixtures.

B. Gibbs-Dalton Law

Perfect gas mixtures are traditionally treated using the Gibbs-Dalton law, wherein each of the individual species components are assumed to occupy the entire volume and each component exerts a partial pressure. The species partial density is then given by:

$$\rho_m = \frac{m_m}{V} \quad (3)$$

where m_m is the mass of species m and V is the total volume. The sum of the partial pressures yields the local pressure of the mixture:

$$p = \sum_N p_m \quad (4)$$

In the case of thermal equilibrium, all components are assumed to be at the same temperature:

$$T = T_1 = T_2 = \dots = T_N \quad (5)$$

Using the perfect gas law, we then have:

$$\rho_m = \frac{p_m M_m}{R_u T} \quad (6)$$

Finally, the mixture density follows from the above relations:

$$\frac{\rho}{M} = \sum_N \frac{\rho_m}{M_m} \quad (7)$$

where the mixture molecular weight is:

$$\frac{1}{M} = \sum_N \frac{Y_m}{M_m} \quad (8)$$

and $Y_m = m_m/m_{mix}$ is the mass fraction of species m . From the above, we can also write the mixture density using an overall equation of state, that can be written as:

$$\rho = \frac{pM}{R_u T} \quad (9)$$

We can readily see that Dalton's law is particularly suited for handling perfect gas mixtures, but it is not convenient for expressing species components that are governed by arbitrary equations of state or for liquid phases. We next consider Amagat's law, which we will see allows for more general representations of the species components.

C. Amagat's Law

An alternate representation of mixtures is given by Amagat's law, wherein each component is taken to occupy a partial volume with a common pressure at the interface. The sum of the partial volumes yields the total volume of the mixture. Amagat's model is typically used for liquid-vapor mixtures, where it is convenient to work in terms of volume fractions. Moreover, the model is equally capable of representing perfect gas mixtures and yields precisely the same results as Dalton's law. Finally, the model is capable of handling arbitrary equations of state. For these reasons, the Amagat model provides the ideal basis for a unified formulation. Amagat's law leads to a different definition of the partial density, namely the mass of species (or phase) m divided by the volume of species (or phase) m . Thus:

$$\tilde{\rho}_m = \frac{m_m}{V_m} = \frac{1}{v_m} \quad (10)$$

where v_m represents the specific volume. Note that the tilde on the partial densities are used to distinguish these definitions from the partial densities defined by Dalton's law.

Each of the phases is taken to be at the same temperature and pressure. Thus, the individual phasic densities can be specified by their independent equations of state as follows:

$$\tilde{\rho}_m = \tilde{\rho}_m(p, T) \quad (11)$$

Since the total volume is given by the sum of the partial volumes, we can write the mixture specific volume as:

$$v = \sum_N Y_m v_m \quad (12)$$

From which, it follows that the mixture density can be written as:

$$\frac{1}{\rho} = \sum_N \frac{Y_m}{\tilde{\rho}_m} \quad (13)$$

It is straightforward to see that Amagat's law yields the same expression for the mixture density as Dalton's law when applied to perfect gas mixtures. For instance, substituting perfect gas equations of state into the above expression, we get:

$$\frac{1}{\rho} = \sum_N \frac{Y_m R_u T}{p M_m} = \frac{R_u T}{p M} \quad (14)$$

Thus, Amagat's law yields identical results as Dalton's law for perfect gas mixtures, but it is also applicable to more general equations of state as well as to liquid mixtures. The above formulation is therefore completely general for arbitrary liquid-gas mixtures and, in combination with the equations of motion, it represents a unified formulation for multi-species and multi-phase flows.

Further, in order to close the system of equations, we also need to express general thermodynamic state relations for the enthalpy:

$$h_m = h_m(p, T) \quad (15)$$

and the mixture enthalpy is given as:

$$h = \sum_N Y_m h_m \quad (16)$$

Finally, we also note the following definition:

$$\rho Y_m = \tilde{\rho}_m \alpha_m \quad (17)$$

where $\alpha_m = v_m/V$ are the volume fractions. Using these definitions, the governing equations may alternately be expressed in terms of the volume fraction. Note also that:

$$\sum_N \alpha_m = 1 \quad (18)$$

The mixture density may also be written as:

$$\rho = \sum_N \tilde{\rho}_m \alpha_m \quad (19)$$

This latter definition is useful when working in terms of the volume fraction variables rather than the mass fraction variables.

D. Mixture Property Derivatives

Given the general forms of the equations of state for the component species (which may be liquid or gas), we can then obtain the properties of the mixture using Eqns. 13 and 16. The general formulation further requires the specification of various property derivatives. We will later see that such properties are necessary for determining various thermodynamic properties of the mixture, such as the speed of sound.

The thermodynamic property derivatives for the arbitrary fluid mixture are defined as:

$$\begin{aligned}\rho_p &= \frac{\partial \rho}{\partial p} & \rho_T &= \frac{\partial \rho}{\partial T} & \rho_{Y_n} &= \frac{\partial \rho}{\partial Y_n} \\ h_p &= \frac{\partial h}{\partial p} & h_T &= \frac{\partial h}{\partial T} & h_{Y_n} &= \frac{\partial h}{\partial Y_n}\end{aligned}\quad (20)$$

The property derivatives can be readily obtained from the equations for the mixture density (Eqns. 13) and mixture enthalpy (Eqn. 16). Thus,

$$\frac{\partial \rho}{\partial p} = \rho \sum_N \frac{\alpha_m}{\tilde{\rho}_m} \frac{\partial \tilde{\rho}_m}{\partial p} = \rho^2 \sum_N \frac{Y_m}{\tilde{\rho}_m^2} \frac{\partial \tilde{\rho}_m}{\partial p} \quad (21)$$

$$\frac{\partial \rho}{\partial T} = \rho \sum_N \frac{\alpha_m}{\tilde{\rho}_m} \frac{\partial \tilde{\rho}_m}{\partial T} = \rho^2 \sum_N \frac{Y_m}{\tilde{\rho}_m^2} \frac{\partial \tilde{\rho}_m}{\partial T} \quad (22)$$

$$\frac{\partial \rho}{\partial Y_n} = \rho^2 \left(\frac{1}{\tilde{\rho}_N} - \frac{1}{\tilde{\rho}_n} \right) \quad (23)$$

$$\frac{\partial h}{\partial p} = \sum_N Y_m \frac{\partial h_m}{\partial p} \quad (24)$$

$$\frac{\partial h}{\partial T} = \sum_N Y_m \frac{\partial h_m}{\partial T} \quad (25)$$

$$\frac{\partial h}{\partial Y_n} = h_n - h_N \quad (26)$$

The individual liquid and gas-phase property derivatives are obtained from their respective equations of state (Eqn. 11 and 15).

Finally, we note that the physical sound speed is specified by:

$$c^2 = \frac{1}{(\partial \rho / \partial p)_s} = \frac{\rho h_T}{\rho \rho_p h_T + \rho_T (1 - \rho h_p)} \quad (27)$$

which in turn yields the following mixture rule:

$$\frac{1}{c^2} = \rho \sum_N \frac{\alpha_m}{\tilde{\rho}_m} \frac{1}{c_m^2} = \rho^2 \sum_N \frac{Y_m}{\tilde{\rho}_m^2} \frac{1}{c_m^2} \quad (28)$$

where the individual phasic sound speeds are defined in the usual manner:

$$c_m^2 = \frac{1}{(\partial \tilde{\rho}_m / \partial p)_s} \quad (29)$$

As before, these can be determined from their respective equations of state (Eqn. 11 and 15).

E. Source Terms

Our interest in multi-phase and multi-species flows typically involves engineering problems that are characterized by gas-phase chemical reactions and/or liquid-gas phase-change. We may express such source terms in the following general form:

$$H = \begin{pmatrix} 0 \\ 0 \\ 0 \\ \dot{w}_m \end{pmatrix} \quad (30)$$

The source term in chemically reacting flows is traditionally written in the Arrhenius form:

$$\dot{w}_m = M_m \sum_{n=1}^{NR} (\dot{c}_m)_n \quad (31)$$

where NR is the total number of reactions. $(\dot{c}_m)_n$ is the rate of production of moles of species m by reaction n ,

$$(\dot{c}_m)_n = (\nu_{mn}'' - \nu'_{mn})(k_{fn} \prod_{l=1}^N C_l^{\nu'_{ln}} - k_{bn} \prod_{l=1}^N C_l^{\nu''_{ln}})$$

where the m^{th} reaction is written as:

$$\sum_{m=1}^N \nu'_{mn} M_m \rightleftharpoons \sum_{m=1}^N \nu''_{mn} M_m$$

Here, ν'_{mn} and ν''_{mn} are the stoichiometric coefficients for the m^{th} species, k_{fn} and k_{bn} are the forward and backward reaction rates. Finally, C_m is the molar concentration of the species and is given by $C_m = \frac{\rho Y_m}{M_m}$.

Phase-change source terms for the vapor may be defined in a phenomenological fashion as:

$$\dot{w}_v = \dot{m}_v^+ + \dot{m}_v^- \quad (32)$$

where the two terms represent the production and destruction of the vapor phase or, conversely, the destruction and production of the liquid phase. The liquid-destruction/vapor-production term is defined as:

$$\dot{m}_l^- = -\dot{m}_v^+ = C_{dest} \frac{\alpha_l \tilde{\rho}_l * min((p - p_s), 0)}{\frac{1}{2} \rho_\infty U_\infty^2 t_\infty} \quad (33)$$

and the liquid production/vapor-destruction term may be written as:

$$\dot{m}_l^+ = -\dot{m}_v^- = C_{prod} \frac{\alpha_v \tilde{\rho}_v * max((p - p_s), 0)}{\frac{1}{2} \rho_\infty U_\infty^2 t_\infty} \quad (34)$$

In the above equations, p_s is the saturation pressure of the liquid-vapor system, which in general is a function of the temperature, and t_∞ is a characteristic convective time scale. Details on the selection of the time scale and the other constants are provided elsewhere.⁹

F. Diffusion Terms

The diffusion terms in the equations of motion take their usual forms for multiple gaseous species. However, for liquid species the phasic mass diffusion terms are usually set to zero because their inclusion would lead to excessive smearing of the liquid-vapor interface, especially in turbulent flow.⁷

III. Computational Formulation

A. Pseudo-Time Framework

Efficient and accurate solution of the multi-phase system requires the use of a pseudo-time-iterative framework for formulating the discrete fluxes and the iterative solution. For effective performance of all fluids and all speeds, we employ preconditioning of the pseudo-time, which insures proper conditioning of the underlying system of equations.^{5,9} We further note that the introduction of the pseudo-time level is a numerical iterative device and is distinct from the physical time stepping that is performed for advancement of the time-accurate solution. The resulting scheme is therefore often referred to as dual-time-stepping, with the physical time advancing the unsteady solution and the pseudo-time introducing non-linear relaxation of the solution.

The preconditioned dual-time framework can be expressed as:

$$\Gamma_p \frac{\partial Q_p}{\partial \tau} + \frac{\partial Q}{\partial t} + \frac{\partial E_i}{\partial x_i} = H + \frac{\partial V_i}{\partial x_i} \quad (35)$$

where the new terms are defined as:

$$Q_p = \begin{pmatrix} p \\ u_j \\ T \\ Y_m \end{pmatrix} \quad \Gamma_p = \begin{pmatrix} \rho'_p & 0 & \rho_T & \rho_{Y_n} \\ u_j \rho'_p & \rho \delta_{jk} & u_j \rho_T & u_j \rho_{Y_n} \\ h_0 \rho'_p - (1 - \rho h_p) & \rho u_k & \rho h_T + h_0 \rho_T & \rho h_{Y_n} + h_0 \rho_{Y_n} \\ Y_m \rho'_p & 0 & Y_m \rho_T & \rho \delta_{mn} + Y_m \rho_{Y_n} \end{pmatrix}$$

In the above matrix, h_0 is the total enthalpy and the term ρ'_p represents the scaled pseudo-property that is responsible for proper conditioning of the system. The definition of this term is considered in the following section.

B. Eigenvalues

The Jacobian of the system given in Eqn. 35 is given by:

$$A_i = \begin{pmatrix} u_i \rho_p & \rho & u_i \rho_T & u_i \rho_{Y_n} \\ \delta_{ij} + u_i u_j \rho_p & \rho u_i (1 + \delta_{ij}) & u_i u_j \rho_T & u_i u_j \rho_{Y_n} \\ \rho u_i h_p + u_i h_0 \rho_p & \rho (h_0 \delta_{ij} + u_i u_j) & \rho u_i h_T + u_i h_0 \rho_T & \rho u_i h_{Y_n} + u_i h_0 \rho_{Y_n} \\ u_i Y_m \rho_p & \rho Y_m \delta_{ij} & u_i Y_m \rho_T & \rho u_i \delta_{mn} + u_i Y_m \rho_{Y_n} \end{pmatrix} \quad (36)$$

The eigenvalues of the preconditioned system are the eigenvalues of $\Gamma_p^{-1} A_p$:

$$\lambda(\Gamma_p^{-1} A_i) = u_i, \lambda_{\pm} \quad (37)$$

where

$$\lambda_{\pm} = \frac{1}{2} \left[u_i \left(1 + \left(\frac{c'}{c} \right)^2 \right) \pm \sqrt{\left(u_i^2 \left(1 - \left(\frac{c'}{c} \right)^2 \right)^2 + 4c'^2 \right)} \right]$$

The new term, c' is the so-called preconditioned sound speed and is defined as:

$$c'^2 = \frac{\rho h_T}{\rho \rho'_p h_T + \rho_T (1 - \rho h_p)} \quad (38)$$

As mentioned earlier, the preconditioned sound speed (c') is selected to insure proper conditioning of the underlying characteristics. In general, the definition is given by:

$$c'^2 = \text{Min}(V_p^2, c^2) \quad (39)$$

and V_p is the velocity scale appropriate to the controlling physics. More details on the definition of the preconditioning velocity scale, V_p , are given elsewhere.^{5,9} Once the preconditioned sound speed is determined, Eqn. 38 is employed to define the property parameter, ρ'_p :

$$\rho'_p = \frac{1}{c'^2} - \frac{\rho_T (1 - \rho h_p)}{\rho h_T} \quad (40)$$

Note that in the absence of preconditioning, $\rho'_p = \rho_p$ and $c' = c$. Then the above eigenvalues reduce to their standard physical values, viz., $u_i, u_i \pm c$.

C. Computational Code

The computational framework is implemented into two general purpose codes. The first is an in-house research code called GEMS—Generalized Equations and Mesh Solver.¹⁶ It is an unstructured upwind finite-volume code that is capable of handling arbitrary fluids governed by generalized state relations. It utilizes line Gauss-Seidel iterations for the inversion of the implicit operator. The second code is UNCLE-M,^{7,12–14} which is a multi-phase code that is based upon the UNCLE code.¹⁷ UNCLE-M is a structured finite-volume code, which utilizes point Gauss-Seidel relaxations for the implicit solver.

IV. Representative Results

We present results for several representative test cases, which are selected to demonstrate the ability of the unified formulation to simulate multi-phase flows, real-gas flows, multi-species flows and a combination of all these effects. The particular examples include cavitating flow around a NACA0015 hydrofoil, real gas effects in an argon nozzle, gaseous hydrogen-oxygen combustion in a uni-element injector and multi-phase/multi-species flow in an underwater rocket plume.

A. Cavitating Flow Around a NACA0015 Hydrofoil

The first test case is that of cavitating water flow around a NACA0015 airfoil. This case is part of a benchmark test case.¹⁸ A sketch of the geometry and flow conditions is given in Fig. 1. The hydrofoil is part of a rectangular wing placed in a water tunnel at an angle of attack of 4 degrees. In the cavitating case, a cavitation bubble is formed on the low-pressure leeward side of the hydrofoil. Experimental data exists for both non-cavitating and cavitating flow conditions¹⁹ and are used to validate the numerical results.

The numerical computations are carried out using our in-house research code GEMS.¹⁶ The flow is assumed to be two-dimensional. A hybrid structured/unstructured grid is used with about 100,000 grid elements. Figure 2 shows the details of the grid near the leading and trailing edges of the hydrofoil. Strong clustering is adopted in the near-body region to capture the vapor cavity as well as viscous and turbulent effects.

The equations of state for water and water vapor are chosen as a unified formula:

$$\tilde{\rho}_m = \tilde{\rho}_{0m} + \frac{Z_m M_m p}{R_u T} \quad (41)$$

where the subscript m stands for either liquid or vapor. For liquid water, $\rho_0 = 1000 \text{ kg/m}^3$ and $Z = 0.0624$, while for water vapor, $\rho_0 = 0$ and $Z = 1$. Likewise, the caloric equation for liquid and vapor is:

$$h_m = h_{0m} + C_{pm}(T - T_{ref}) \quad (42)$$

where $h_0 = 112.75 \text{ kJ/kg}$ and $C_p = 4180 \text{ J/kg} - K$ for liquid water and $h_0 = 2796 \text{ kJ/kg}$ and $C_p = 2050.8 \text{ J/kg} - K$ for water vapor. Under these circumstances, the speed of sound in liquid water at the inlet flow condition is 1481 m/s.

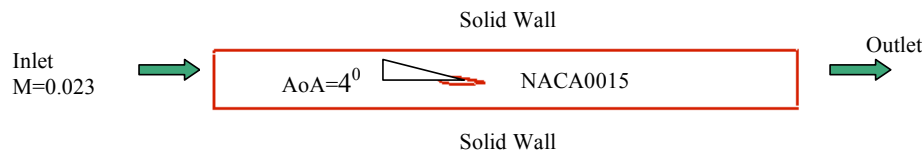


Figure 1. Sketch of computational domain showing boundary conditions.

Both non-cavitating and cavitating cases were computed and compared with existing experimental data. The non-cavitating case corresponds to a higher inlet pressure of $0.59 \times 10^5 \text{ Pa}$, while the cavitating case is at a lower inlet pressure of $0.12 \times 10^5 \text{ Pa}$. The inlet Mach numbers in both cases is about 0.002. Figure 3 shows plots of the pressure coefficient for both cases. In the non-cavitating case, the current computational predictions are also compared with a 2D potential flow solution in addition to the experimental data. Good overall agreement is observed between the predictions and the reference data in both cases. As expected, there is some discrepancy observed in the cavitating case near the trailing edge of the cavitation bubble. The inherently unsteady nature of the flow in this region makes it a challenge for both the experiments and the simulations.

Figure 4 shows flowfield contours for the cavitating case. In (a), the vapor volume fraction distribution is shown to indicate the extent of the cavitation zone on the hydrofoil surface. The vapor volume fraction contour value of 0.5 is selected to demarcate the cavitation bubble boundary and also to determine the length of the cavitation bubble. The corresponding bubble length is determined to be about 0.4 times the chord length, which is also in reasonable agreement with the experimental data of 0.397-0.464 times the chord length. The iso-contours of density are shown in (b), wherein the high density ratio between the liquid

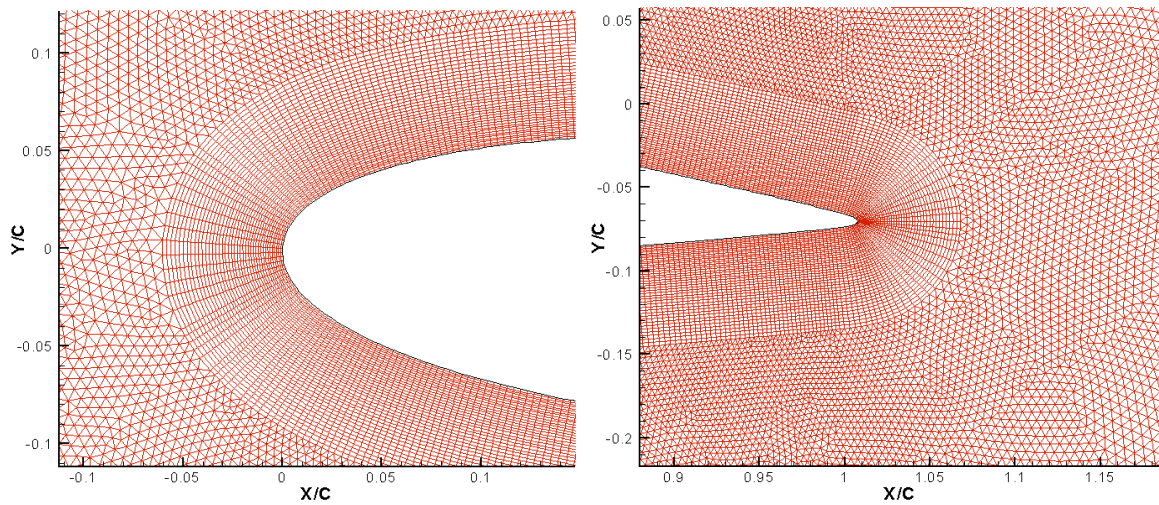


Figure 2. Structured/unstructured hybrid grid details near leading (left) and trailing edge (right) of NACA0015 hydrofoil.

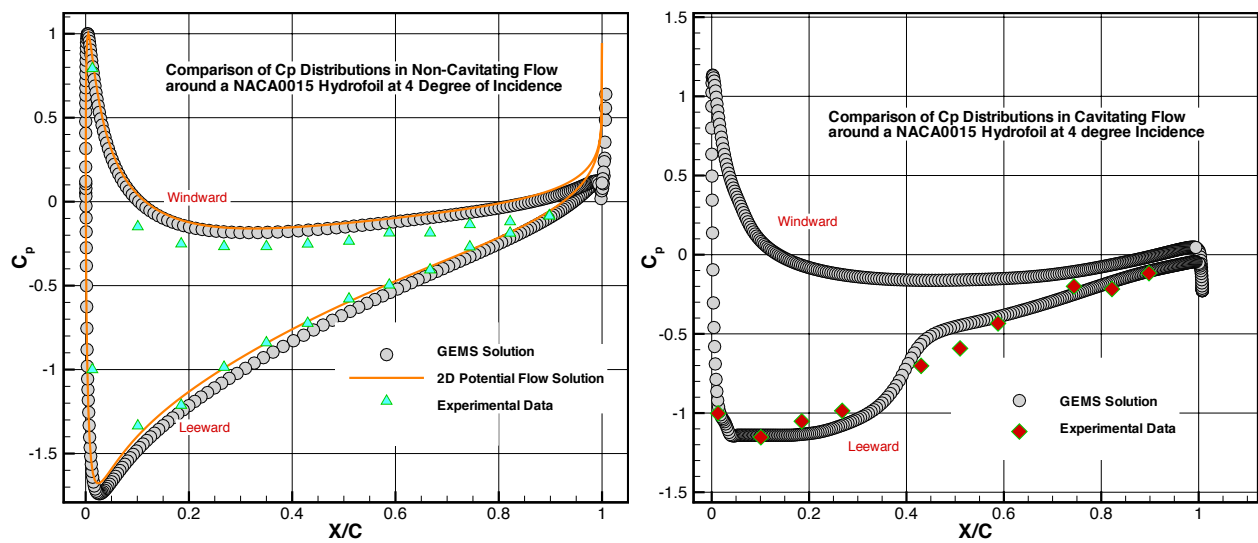


Figure 3. Comparison of experimental and computed data for C_p around hydrofoil for non-cavitating (left) and cavitating (right) cases.

and vapor regions is clearly evident. Finally, Mach number contours are presented in(c). Because of the very low mixture sound speed, the local Mach number in the interface region is observed to reach almost unity. The flowfield is then comprised of incompressible flow in the free-stream, low Mach compressible flow in the cavitation bubble and transonic flow in the two-phase mixture region. Thus, the present formulation is capable of handling such strong density and Mach number variations in the the same flowfield.

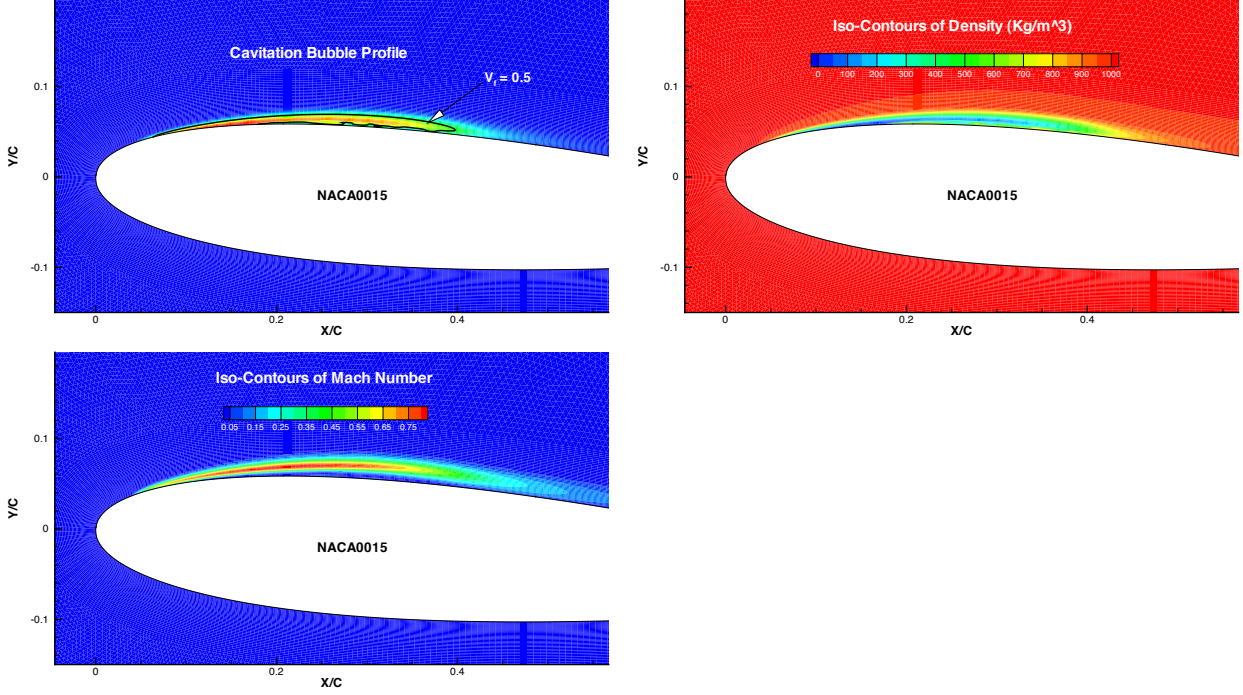


Figure 4. Flowfield contours for cavitating NACA0015 hydrofoil case: (a) cavitation bubble profile, (b) Density contours, (c) Mach number contours.

B. Real Gas Effects in Argon Nozzle Flows

As the next example, we present computations for the two-phase flow of argon through the concentric, dual annular nozzle arrangement shown in Fig. 5. Supersonic streams enter through the two divergent nozzle sections from the left and expand separately before merging in a common evacuated chamber downstream of the nozzles. The colors in the figure indicate the manner in which the 150,000 cells used to model the flowfield are partitioned for parallel cluster computation.

For this calculation, we use real gas properties for argon, taken from the REFPROP database. Argon is a noble gas that exhibits ideal gas behavior at all temperatures and pressures (except for ultra-high temperatures where ionization is present), until it reaches the condensation or sublimation line at sufficiently low temperatures. For the cases of interest here, the upstream pressures is 50 kPa in the outer nozzle and 30 kPa in the inner nozzle. The upstream stagnation temperature of both streams is 300 K. The downstream exit pressure in the chamber is set to 10^{-7} kPa. At these conditions, the fluid crosses the condensation and sublimation lines so that two-phase flow may be expected in the chamber.

The vapor-liquid condensation line and the sublimation line for argon are plotted on the p-T diagram in Fig. 6 and are given algebraically by:

$$\ln\left(\frac{P_s}{P_c}\right) = \frac{T_c}{T} \left[a_1 \left(1 - \frac{T}{T_c}\right) + a_2 \left(1 - \frac{T}{T_c}\right)^{2.7} \right] \quad (43)$$

where $T_c = 83.8058$ K and $P_c = 68.891$ kPa represent the critical pressure and temperature for argon, while $a_1 = -11.391604$ and $a_2 = -0.39513431$.

To simulate the condensation process, we treat each phase as a separate species and implement a simple non-equilibrium phase-change model for the rate of production of the condensate:

$$\dot{m}_l^+ = C_{prod}\rho Y_v \max(P - P_s(T), 0) \quad \dot{m}_l^- = C_{dest}\rho Y_l \min(P - P_s(T), 0) \quad (44)$$

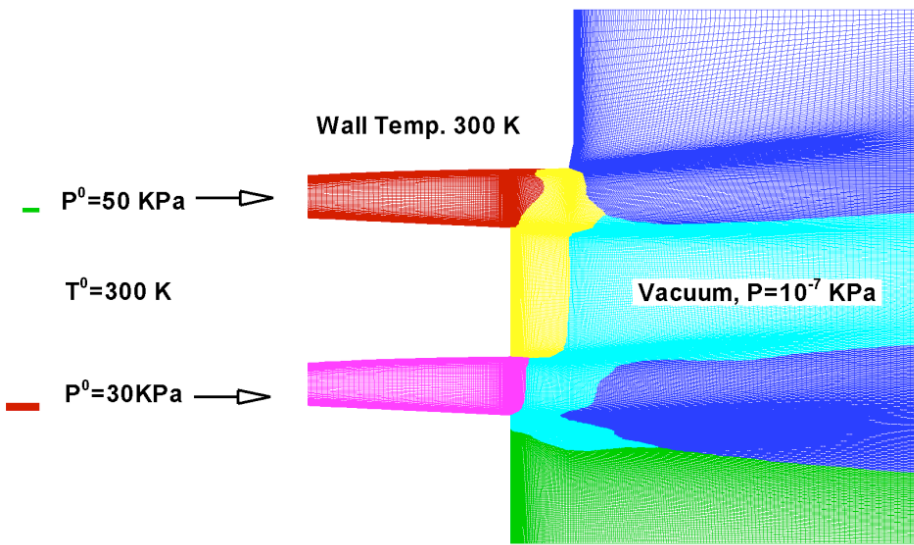


Figure 5. Geometry and inlet flow conditions of PRS nozzle with 10 partitions of computational domain represented by different colors.

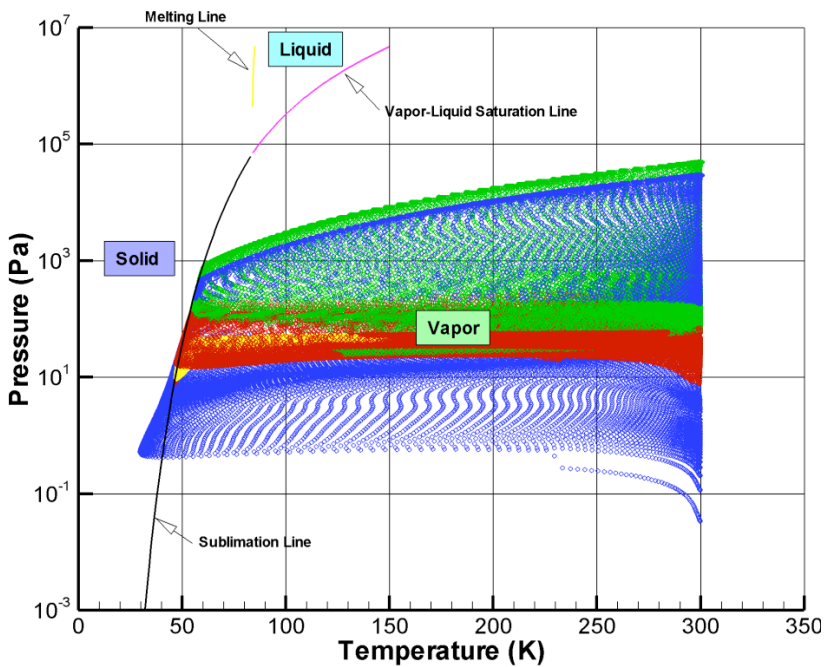


Figure 6. Pressure-temperature curves for two-phase argon nozzle flow. Colors represent the data from the different partition zones of the computational domain

Here, the quantities, C_{prod} and C_{dest} , are scaling constants, which correspond to inverse time constants for production and destruction of the liquid phase. Thus, faster the transition time, the larger the values of these constants. In the present study values in the range of 20-200 were used. The former indicates partial condensation, while the latter indicates almost complete condensation in the plume region.

Computational results for the fastest transition case ($C_{prod} = 200$) are considered next. Figure 6 shows the states occupied by the fluid during various stages of the nozzle flow. The fluid states are shown color coded as per the grid plot in Fig. 5. Figure 7 shows corresponding temperature and liquid mass fraction contours for the fastest transition case. It is evident that considerable condensation occurs and the minimum temperature is around 50 K, indicating strong thermal effects in the phase change process.

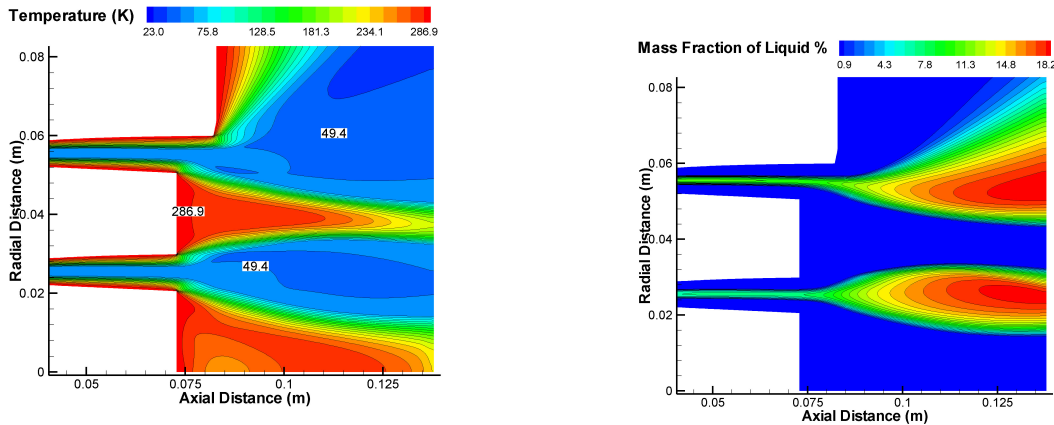


Figure 7. Temperature and mass fraction contours for two-phase argon flow in nozzle.

Finally, Fig. 8 shows the comparison of the radial density profiles at a given location in the chamber with experimental data. We note that the large change in density across the chamber is reasonably well captured by the phase change model. These results demonstrate that the present method is indeed capable of handling phase-change effects in the presence of significant thermal effects.

C. Hydrogen-Oxygen Unielement Injector

As a third test case, we consider the application of the unified formulation to gaseous mixtures and chemically reacting flows. As a specific example, we consider the H_2/O_2 shear co-axial injector experiments in an optically accessible rocket chamber.²⁰ Figure 9 shows the computational domain corresponding to the experiments. Gaseous oxygen enters through the central port and gaseous hydrogen through the annulus of the shear coaxial injector. The overall chamber diameter is 50.8 mm, while the injector core diameter is 7.75 mm and injector outer diameter is 12.7 mm. The inlet velocity for the oxygen stream is 57 m/s and for the hydrogen stream is 171 m/s. The overall O/F ratio is 4. The chamber pressure is 1.31 MPa. Both gases are specified to be at an inlet temperature of 300 K. The gases mix and react in the combustion chamber and the products of combustion are exhausted through a choked nozzle. The computational study employs nine gaseous species and eighteen chemical reactions to represent the combustion process. Additional details of related computational studies are given elsewhere.^{21,22}

Figure 10 shows the comparison of the predicted and experimental radial profiles of the axial velocity component at several stations downstream of the injector. Considering the complexity of the reacting flowfield, the agreement is fairly good. It is interesting that, in the near-injector stations, the computations predict less diffusion of the velocity profile than the experiments do. This discrepancy is possibly due to the lack of a turbulent combustion model in the present analysis, which could be responsible for greater spreading of the combustion zone and thus give rise to increased diffusion.

Comparisons of radial profiles of the oxygen and hydrogen mole fractions with experimental data for an O/F ratio of 4 are shown at several axial stations in Figs. 11 and 12. At the near-injector location of $x = 1$ inch, very good agreement of the predictions with measurements is observed. At the second location at $x = 2$ inches, the agreement is still fairly good; however, the computed profiles show slightly higher levels

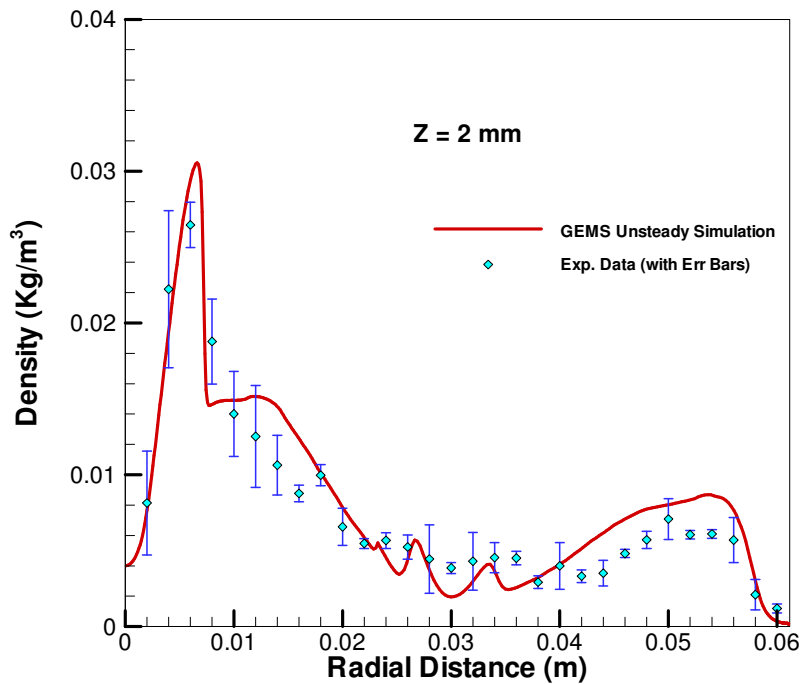


Figure 8. Comparison of predicted radial density profiles with experimental data.

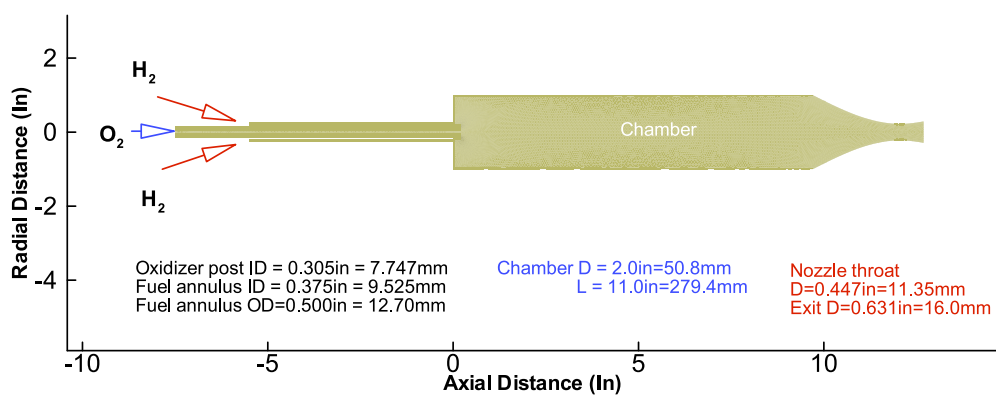


Figure 9. Schematic of gaseous hydrogen-gaseous oxygen uni-element shear co-axial injector, combustor and nozzle configuration.

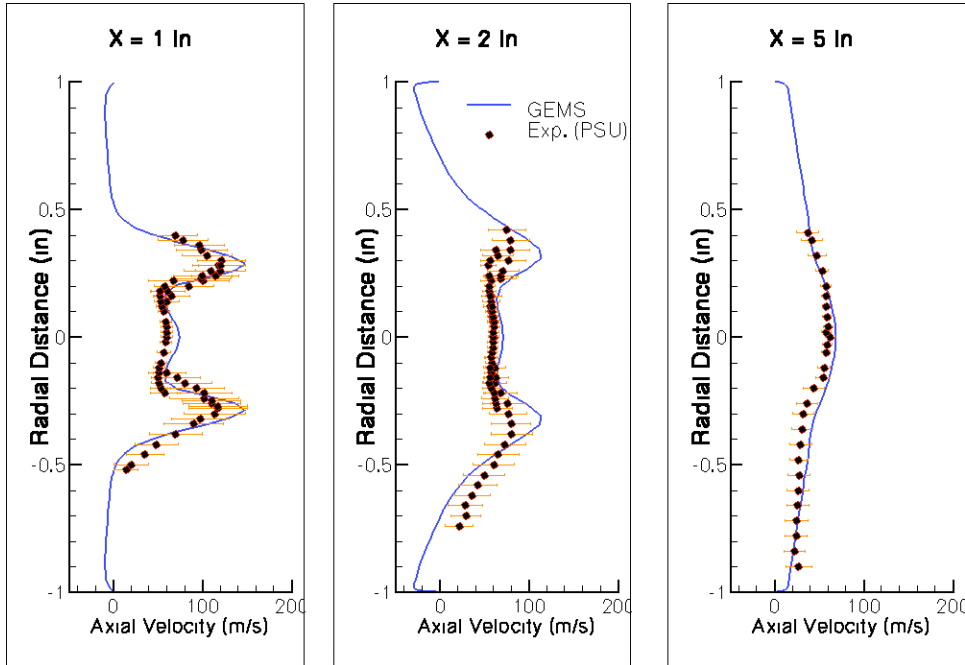


Figure 10. Comparison of predicted and experimental radial profiles of the axial velocity component at several stations downstream of the injector.

of combustion than the measurements. At the final location of $x = 5$ inches, which is close to the computed edge of the flame, the hydrogen and oxygen mole fractions show significant discrepancy suggesting that the computations are predicting lower levels of combustion. As before, the computations are also observed to predict lower levels of radial diffusion at the edges of the flame.

D. Notional Underwater Propulsion Plume

As a final example, we present preliminary computational results of an underwater propulsion plume flowfield that is comprised of multiple gas species and liquid-vapor mass transfer. The application involves supersonic exhaust flow in the propulsion plume, while the vehicle travels at low subsonic Mach numbers in liquid water. Figure 13 depicts a notional supercavitated vehicle (not part of the calculation) that is pictured on the left, and a sample computational grid of the propulsion plume flowfield. The inflow consists of three separate streams. The propulsion stream consists of 90 % steam, 9 % air, and 1 % liquid water (by volume) at 400 K and 199 kPa and emerges from the end of the blast tube at 1000 m/s flowing to the right into the domain at a Mach number of approximately 7. Surrounding the propulsion stream is the ventilated cavity flow that enshrouds most of the super-cavitated torpedo. This stream is comprised of 49 % steam, 49 % air, and 2 % liquid water (by volume) at 300 K and 50 m/s and a Mach number of 0.536. The third stream that surrounds the cavity flow is the free-stream liquid water flow, which enters the domain at the same velocity and temperature as the cavity flow but has a Mach number of 0.0344.

For liquid water, we apply the modified Tait equation of state as presented by Neaves and Edwards.¹¹ The saturation pressure of water and steam is a function of temperature and is based on the Oldenbourg saturation equations.¹¹ The gases, air and steam, are modeled as ideal, air with $\gamma = 1.4$ and $C_p = 1003.5\text{J}/(\text{kg} - \text{K})$, steam with $\gamma = 1.327$ and $C_p = 1872.9\text{J}/(\text{kg} - \text{K})$. The calculations are performed with the UNCLE-M code^{7, 12-14} using the unified formulation developed in the present work.

Figure 14 shows the computed mixture density and pressure contours, while Fig 15 shows the associated temperature and Mach number contours. The solution is axisymmetric, and the plots are mirrored about the symmetry axis for illustrative purposes. The mixture density of the solution reveal the clear demarcation between the high density free-stream water (shown as red) and the low-density propulsion and cavity streams (shown as blue). Note the initial contraction of the low density region due to the acceleration of and condensation in the supercavity stream, followed by widening due to the shock and the deceleration of the

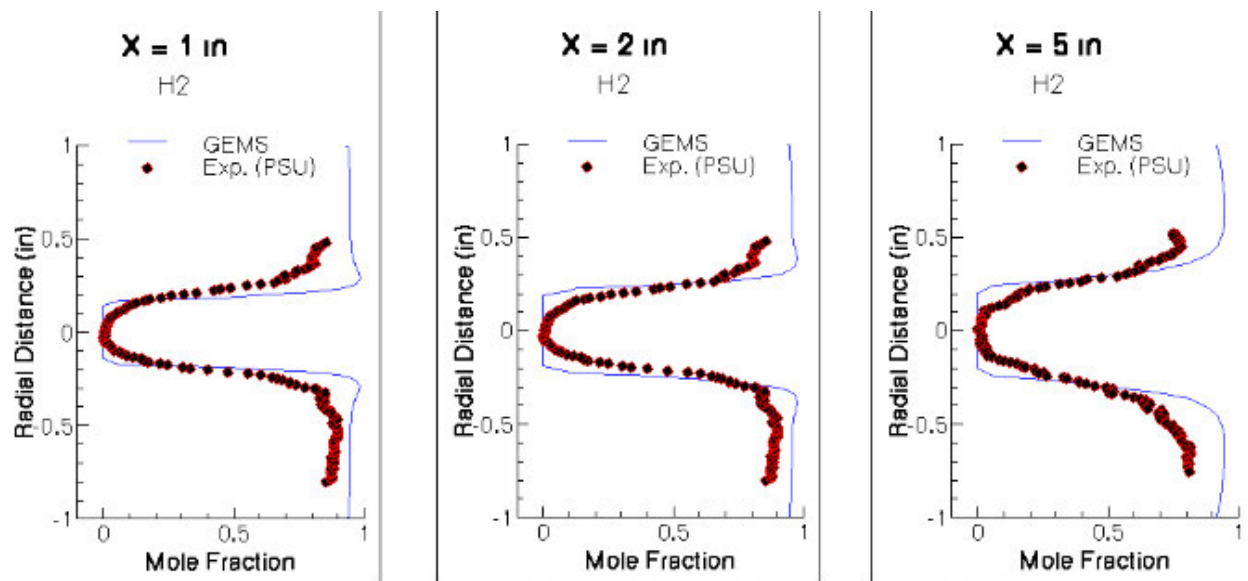


Figure 11. Comparison of predicted and experimental radial profiles of the hydrogen mole fraction at several stations downstream of the injector.

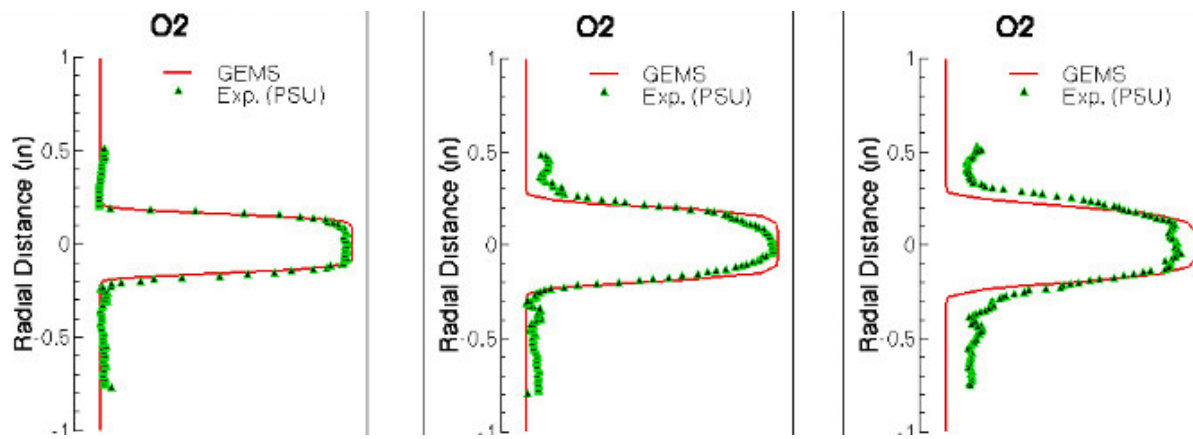


Figure 12. Comparison of predicted and experimental radial profiles of the oxygen mole fraction at several stations downstream of the injector.

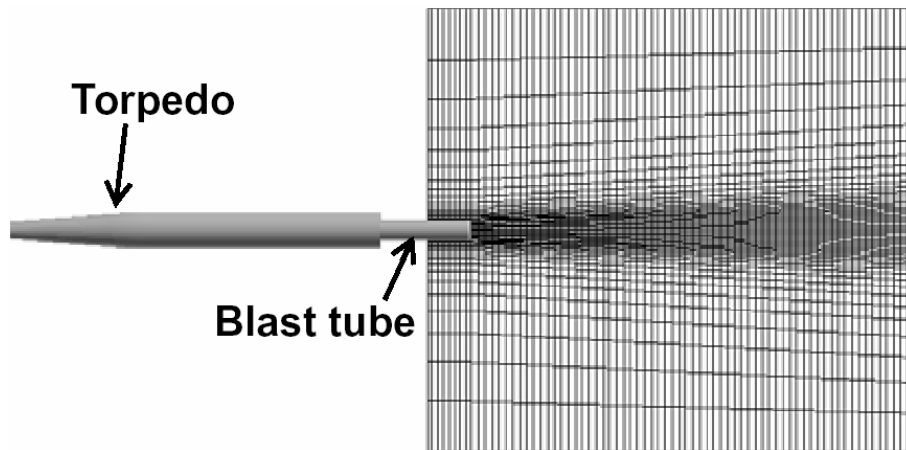


Figure 13. Notional torpedo and computational grid (with every other point removed).

supersonic core. The pressure contours reveal the familiar expansion pattern of the propulsion stream and the subsequent shock system. The temperature field shows the high temperature propulsion stream surrounded by the cooler surrounding flow. The expansion and shock pattern of the core stream is also apparent in the temperature field. Finally, the Mach number contours reveal the high supersonic core of the plume, the transonic Mach number of the two-phase mixture region and the low Mach number of the surrounding liquid flow.

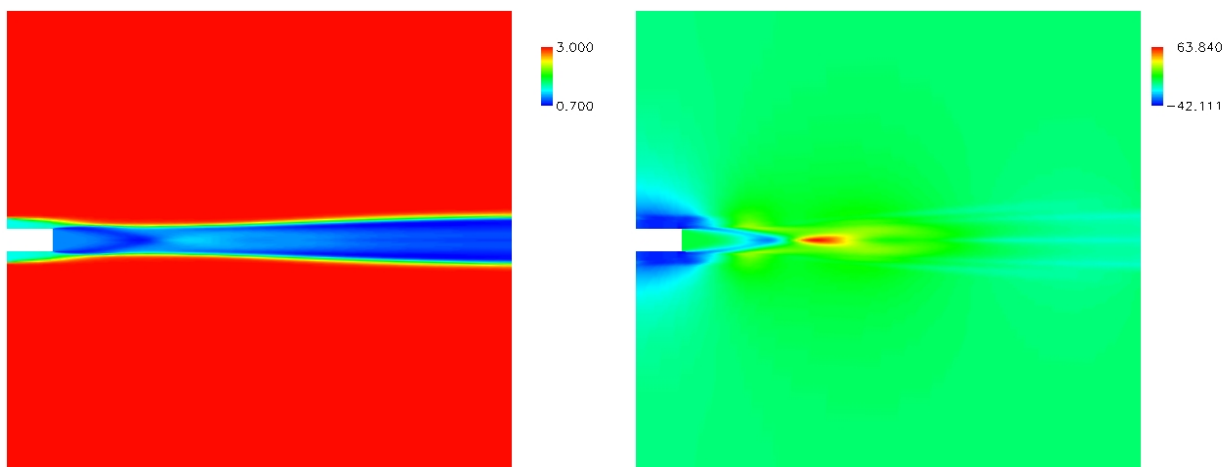


Figure 14. Contours of the log of the density and pressure in underwater plume flowfield involving mixture of water, steam and air.

The above results confirm the ability of the unified formulation to handle multiple gaseous species and multiple-phases in the same flowfield. Future studies will involve more detailed studies of the plume flowfield including the effects of chemical reactions in the plume.

V. Summary

Many engineering problems involve multi-phase or multi-species effects that occur independently as in cavitation, condensation and gas-phase reacting flows. In certain cases, these effects may also occur simultaneously in the same flowfield: examples are underwater rocket propulsion or spray combustion. Traditional approaches for solving these problems have relied upon distinct computational formulations which are difficult to adapt and modify for different circumstances. We have developed a unified computational framework

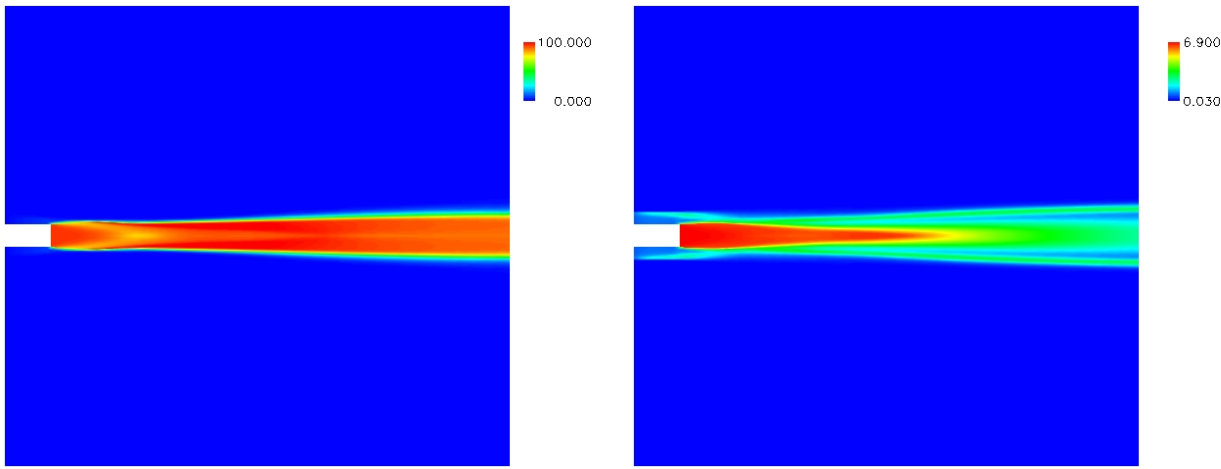


Figure 15. Contours of the temperature and Mach number in underwater plume flowfield involving mixture of water, steam and air.

that is capable of handling homogeneous mixtures of multiple gaseous species, multiple phases and fluids following arbitrary (or real gas) equations of state. Our approach is based upon uniformly using mass fraction variables for all species and phases and Amagat's mixture law for developing the thermodynamic state of the mixture. Amagat's law provides a more convenient basis for unification than Gibbs-Dalton law since the latter is easy to apply only for certain forms of the equation of state (such as the perfect gas EOS). Further, we combine the unified formulation with a general pseudo-time or preconditioning framework, that provides uniformly accurate and efficient computational performance for all fluids and fluid-mixtures.

The broad capabilities of the unified framework are demonstrated using a series of test cases that involve hydrodynamic cavitation, condensation in argon nozzles, gaseous hydrogen-oxygen combustion and underwater rocket propulsion. Each of the examples showcases different practical scenarios: for instance, the cavitation and condensation problems involve multiple phases and phase change, the combustion problem involves multiple species and chemical kinetics, and the underwater rocket flowfield involves both multiple gaseous species and phases. Our results indicate that the proposed formulation is applicable to a wide range of flowfields and provides a convenient framework for general solutions of computational physics flowfields.

Acknowledgments

Dr. Venkateswaran Sankaran acknowledges the support of NASA-Ames Research Center, Contract No. NNA04CI36A, with Dr. Goetz Klopfer as contract monitor. Dr. Jay Lindau acknowledges the support of the Office of Naval Research, Grant N00014-01-1-0325, with Dr. Kam Ng as contract monitor.

References

- ¹Y. S. Chen, H. M. Shang, C. P. Chen and T. S. Wang, A Combined Eulerian-VOF-Lagrangian Method for General Gas-Liquid Flow Applications, *Numerical Heat Transfer*, Vol. 30, (1996) 409-422.
- ²K. Premnath and J. Abraham, Discrete Lattice BGK Boltzmann Equation Computations of Transient Incompressible Turbulent Jets, *Int. J. Modern Physics C*, 15(5):699-719, 2004.
- ³Merkle, C. L., Sullivan, J. A. Y., Buelow, P. E. O. and Venkateswaran, S., Computation of Flows with Arbitrary Equations of State, *AIAA Journal*, Vol. 36, No. 4, pp. 515-521, April 1998.
- ⁴Weiss, J. M., Maruszewski, J. P. and Smith, W. A., *AIAA Journal*, Vol. 37, No. 1, pp. 29, 1999.
- ⁵Venkateswaran, S. and Merkle, C. L., "Analysis of Preconditioning Methods for the Euler and Navier-Stokes Equations," 1999-03, *VKI Lecture Series on CFD*, March, 1999.
- ⁶S. Venkateswaran, M. Deshpande and C. L. Merkle, Computation of Turbulent Reacting Flowfields Using the Preconditioned Navier-Stokes Equations, *CFD Journal*, Vol. 8, No. 2, pp. 1978-1985, 1999.
- ⁷Kunz, R.F., Boger, D.A., Stinebring, D.R., Chyczewski, T.S., Lindau, J.W., Gibeling, H.J., Venkateswaran, S., and T.R. Govindan, A Preconditioned Navier-Stokes Method for Two-Phase Flows with Application to Cavitation Prediction, *Computers and Fluids*, Vol. 29, pp. 849-875, November, 2000.
- ⁸Ahuja, V., Hosangadi, A., and S. Arunajatesan, Simulations of Cavitating Flows using Hybrid Unstructured Meshes,

ASME Journal of Fluids Engineering, Vol. 123, No. 2, 2001.

⁹Sankaran, V., Lindau, J.W., Kunz, R.F. and C.L. Merkle, Computation of Multiphase Mixture Flows with Compressibility Effects, *Journal of Computational Physics*, vol. 180, pp. 5477, 2002.

¹⁰Senocak, I. and W. Shyy, A Pressure-Based Method for Turbulent Cavitating Flow Computations, *Journal of Computational Physics*, vol. 176, pp. 363- 383, 2002.

¹¹Neaves, M. D. and Edwards, J. R., Hypervelocity Underwater Projectile Calculations Using a Preconditioning Algorithm, AIAA-2003-1286, *AIAA Aerospace Sciences Meeting and Exhibit*, Reno, NV, 2003.

¹²Lindau, J.W., Sankaran, V., Kunz, R.F. and C.L. Merkle, Development of a Fully-Compressible Multiphase Reynolds-Averaged Navier-Stokes Model, *AIAA CFD Conference*, AIAA 2001-2648, Anaheim, CA, 2001.

¹³Lindau, J.W., Sankaran, V., Kunz, R.F. and C.L. Merkle, Computation of Compressible Multiphase Flows, *AIAA Aerospace Sciences Meeting and Exhibit*, AIAA 2003-1285, January, 2003.

¹⁴Lindau, J.W., Sankaran, V., Kunz, R.F. and C.L. Merkle, Multiphase Computations for Underwater Propulsive Flows, AIAA 2003-4105, *AIAA CFD Conference*, Orlando, FL, June, 2003.

¹⁵Van Wylen, G. J. and R. E. Sonntag, *Fundamentals of Classical Thermodynamics*, SI Version, Third Edition, John Wiley and Sons, 1985.

¹⁶Li, D., Sankaran, V., Fakhari, K. and C.L. Merkle, "Convergence Assessment of General Fluid Equations on Unstructured Hybrid Grids, AIAA CP 2001-2557, *15th AIAA CFD Conference*, Anaheim, CA, 2001.

¹⁷Taylor, L. K., Arabshahi, A., and D.L. Whitfield, Unsteady Three-Dimensional Incompressible Navier- Stokes Computations for a Prolate Spheroid Undergoing Time-Dependent Maneuvers, AIAA Paper 95-0313, 1995.

¹⁸F. Beux, M. V. Salvetti, A. Ignatyev, D. Li, C. Merkle and E. Sinibaldi, A Numerical Study of Non-Cavitating and Cavitating Liquid Flow Around a Hydrofoil, in preparation.

¹⁹E. Raposelli, A. Cervone, C. Bramanti and L. d'Agostino, Thermal Cavitation Experiments on a NACA0015 Hydrofoil, *Proceedings of the FEDSM'03 Fourth ASME/JMSE Joint Fluids Engineering Conference*, Honolulu, Hawaii, July, 2003.

²⁰M.J. Foust, M. Deshpande, S. Pal, T. Ni, C.L. Merkle, and R.J. Santoro, Experimental and Analytical Characterization of a Shear Coaxial Combusting GO 2 /GH 2 Flowfield, AIAA 96-0646, *34th Aerospace Science Meeting and Exhibit*, January 15-18, Reno NV, 1996.

²¹Schley, C.-A., Hagemann, G. Tucker, P.K., Venkateswaran, S., Merkle, C.L., Comparison of Computational Codes for Modeling Hydrogen-Oxygen Injectors, AIAA 97-3302, *33rd AIAA/ASME/SAE/ASEE Joint Propulsion Conference and Exhibit*, Seattle, WA, July 1997.

²²Archambault, M. R., and Peroomian, O., Three-Dimensional Simulations of a Gas/Gas, Hydrogen/Oxygen Engine, AIAA 2003-0314, *41st Aerospace Science Meeting and Exhibit*, Reno, NV, Jan., 2003.